

Spin liquid state in Y-Kapellasite, $Y_3Cu_9(OH)_{19}Cl_8$ by external pressure controlled frustration

Dipranjan Chatterjee^{1,2}, Petr Doležal^{3,4}, Federico Abbruciati⁵, Tobias Biesner⁶, Katharina M. Zoch⁷, Rustem Khasanov⁸, Shams Sohel Islam⁸, Guratinder Kaur⁹, Seulki Roh⁶, Francesco Capitani¹⁰, Gaston Garbarino⁵, Cornelius Krellner⁷, Philippe Mendels¹, Edwin Kermarrec¹, Martin Dressel⁶, Björn Wehinger⁵, Andrej Pustogow⁴, Fabrice Bert¹, and Pascal Puphal^{9,11}

¹Université Paris-Saclay, CNRS, Laboratoire de Physique des Solides, 91405, Orsay, France

²Clarendon Laboratory, Department of Physics, University of Oxford, Parks Road, OX1 3PU, United Kingdom

³Department of Condensed Matter Physics, Faculty of Mathematics and Physics, Charles University, Ke Karlovu 5, 121 16 Prague 2, Czech Republic

⁴Institute of Solid State Physics, TU Wien, 1040 Vienna, Austria

⁵European Synchrotron Radiation Facility, 71 Avenue des Martyrs, F-38043 Grenoble, France

⁶1. Physikalisches Institut, Universität Stuttgart, Pfaffenwaldring 57, 70569 Stuttgart, Germany

⁷Physikalisches Institut, Goethe-Universität Frankfurt, Frankfurt am Main, Germany

⁸Laboratory for Muon-Spin Spectroscopy, Paul Scherrer Institut, 5232 Villigen, Switzerland

⁹Max-Planck-Institute for Solid State Research, Heisenbergstraße 1, 70569 Stuttgart, Germany

¹⁰Synchrotron SOLEIL, L'Orme des Merisiers Départementale 128, 91192 Saint-Aubin, France

¹¹2. Physikalisches Institut, Universität Stuttgart, Pfaffenwaldring 57, 70569 Stuttgart, Germany

ABSTRACT

Magnetic frustration is a key ingredient to prevent conventional ordering and, in combination with enhanced fluctuations in low dimensional quantum magnets, to stabilize the long sought spin liquid ground states. Most experimental spin liquid candidates inevitably deviate from perfectly frustrated models due to chemical and structural disorder, blurring the nature and origin of their ground states. Y-Kapellasite $Y_3Cu_9(OH)_{19}Cl_8$ realizes a chemically clean system with an underlying kagome sub-lattice. The crystals undergo the theoretically predicted magnetic in-plane (1/3 1/3) order from a subtle release of frustration due to a distortion of the kagome system realised by displaced Y atoms. By studying the effect of pressure on the structure and optical phonons, we show that this distortion is partially lifted by compression towards a more isotropic model of interactions, in a gradual manner, without structural transition. Using μ SR, we further show that the magnetic ground state is surprisingly sensitive to the applied pressure for a mineral, and that under a moderate 2 GPa pressure, the frustration increase is sufficient to induce a fluctuating ground state. Suppressing long-range magnetic order via frustration tuning with pressure, in an ultraclean material, establishes a major step towards realizing a well-controlled spin liquid ground state.

Spin liquids (SL) offer a platform for exploring long-range quantum entanglement and fractionalized excitations. While many candidate materials for SLs have been identified, only a few have been thoroughly studied in single-crystal form, and most suffer from varying degrees of disorder. The earliest SL system is the organic triangular lattice compound κ -(BEDT-TTF)₂Cu₂(CN)₃¹. In this material, disorder arises from randomly oriented carbon and nitrogen atoms^{2,3} and Cu²⁺ impurities, introducing charged $S = 1/2$ defects⁴⁻⁶. Next was the kagome system ZnCu₃(OH)₆Cl₂^{7,8} and later ZnCu₃(OH)₆FBr⁹. Here, Zn²⁺ and Cu²⁺ site mixing is recognized^{9,10}, resulting in inhomogeneous dynamics^{9,11}. The triangular lattice compound YbMgGaO₄ displays SL signatures^{12,13}. However, site shared Mg/Ga results in random distribution of Mg²⁺ and Ga³⁺ ions leads to orientational spin disorder¹⁴. In the hyper-kagome lattice SL system Ca₁₀Cr₇O₂₁, Cr⁵⁺¹⁵ mixes with non-magnetic Cr⁶⁺ ions and presents a split atomic Cr position. Lastly, a field-induced Kitaev SL state has been first suggested in honeycomb α -RuCl₃¹⁶, while later it was found that this compound exhibits considerable stacking disorder^{17,18}. Similarly, the Kitaev SL system H₃LiIr₂O₆¹⁹, reveals enormous stacking faults²⁰.

While geometrical frustration has been considered of primary relevance for suppressing long-range order (LRO), disorder appears to be a unifying feature of the prime SL candidates, raising the question of whether randomness may also play an essential role in formation of some SL. Real materials, even in single-crystalline form, deviate from idealized theoretical models as all exhibit some degree of disorder. In order to separate the effects of frustration and randomness, one should investigate systems with the smallest amount of disorder and tune existing LRO within the same single crystal by a nonthermal method.

Some efforts were made in pyrochlores, where via pressure a coexistence of LRO and SL was shown in $\text{Tb}_2\text{Ti}_2\text{O}_7$ ²¹, a transition from SL to FM was observed in $\text{Yb}_2\text{Ti}_2\text{O}_7$ ²² and pressure in $\text{Tb}_2\text{Sn}_2\text{O}_7$ was shown to change the short-range spin correlations and suppress ferromagnetic correlations²³. Pressure was shown to reduce the disorder in RuCl_3 ²⁴ and pressure was applied to $\text{ZnCu}_3(\text{OH})_6\text{Cl}_2$, where the Cu-O-Cu angles are influenced only subtly²⁵ leading to no change in the μSR spectra and hence a continuous SL ground state²⁶ until at 8 GPa a structural transition occurs²⁵. To date, however, no system exhibiting LRO has been shown to transition into a SL state in a combined study of structure and magnetism under application of pressure.

In the present work, we examine the kagome compound $\text{Y}_3\text{Cu}_9(\text{OH})_{19}\text{Cl}_8$ (Y-Kapellasite)²⁷⁻³⁰. Y-Kapellasite shows 1/9 substitution of Cl^- by $(\text{OH})^-$, and due to the shorter Y-O bond these are pulled out of the plane and therefore distort the kagome lattice to an anisotropic models with three exchange interactions shown in Fig. 1. We found that the system undergoes LRO below 2.2 K and via INS we estimated it very close to a SL groundstate²⁹. Via uniaxial-strain we reported the revival of antiferromagnetic order by controlled frustration release³⁰. Subtle disorder already induces a SL as found in powder²⁸ and also appears in the Br counterpart³¹⁻³³, where Y is partially occupied in the plane. In contrast, our $\text{Y}_3\text{Cu}_9(\text{OH})_{19}\text{Cl}_8$ single-crystals contain no site mixing, a stable Cu^{2+} oxidation state, with a clear superstructure, hence resulting in LRO as evidenced by NMR^{29,30}. Here, we study these clean single-crystals under hydrostatic pressure, where the gradual reduction in geometric magnetic frustration leads to a SL ground state at relatively low pressures of around 3 GPa.

Y-Kapellasite crystallizes in the trigonal space group #148 $R\bar{3}$ with $a = b = 11.57 \text{ \AA}$, $c = 17, 33 \text{ \AA}$ with the kagome skeleton shown in Fig. 1b, which is a subgroup and supercell of $\text{YCu}_3(\text{OH})_6\text{Cl}_3$ ¹⁰. We display the zonal (0kl) maps of diffraction of the subcell in red in Fig. S1a, which clearly differ from the supercell (see Fig. S1b,c) independent of pressure. In the supercell, no partial occupancies exist and the Y atoms move out of the kagome plane, leading to a buckling of the kagome realized by two crystallographically inequivalent Cu positions displayed in Fig. 1b. The buckling shortens one of the bonds to 3.26 \AA (Cu1-Cu2 green line in Fig. 1) corresponding to the magnetic exchange path J' , while the others remain around 3.38 \AA . This squeezes the Cu-O-Cu bonding angle to a lower one around 110° , while the others remain at 116° and 117° (see Fig. 2c). The magnetic substructure of the distorted kagome consists of the orange Cu1-Cu1 hexagons with the exchange interactions in orange J_\square linked by the blue J from Cu2-Cu1 and the green J' Cu1-Cu2 bonds. Via DFT these exchange interactions have been determined³⁴, with a remarkably low J' (Fig. 1a black square). Notably, from our INS experiments we estimated larger J' placing us near the phase border of a SL (see Fig. 1a yellow star) with $J_\square=140 \text{ K}$ and J' ranging from 56-70 K, in line with the Curie-Weiss temperature of -100 K ²⁷.

Upon the application of external pressure softer bonds will compress more, whereas already compressed bonds usually are more rigid – which, in the present system, increases frustration and drives the system towards a SL state. Furthermore, pressure will push the Y atoms back into the plane mostly affecting the orange Cu1 defining the largest J_\square . We studied the effect of external pressure application via high-pressure single-crystal XRD. The evolution of the lattice parameters upon pressurization in a diamond anvil cell is summarized in Fig. 2a, yielding a bulk modulus of 80 GPa. The system compresses isotropically and no structural transitions are observed up to 10 GPa, visible by the unchanged (0 k l) zonal map displayed in Fig. S1. According to our assumption, we find that the short Cu1-Cu2 distance (see in Fig. 2b green) changes less than the longer bonds, especially than the Cu1-Cu1 (orange). Similarly, the Cu-O-Cu angles reduce strongly for Cu1-O-Cu1 (orange), while the low Cu1-O-Cu2 stays constant (see Fig. 2b). In oxides the magnetic exchange is driven by superexchange interaction, which depends on the bond angle, which we estimate via the formula

$$J(K) \approx -1270.5 + 12 \cdot \phi \quad (1)$$

(see supplemental material and Fig.S2 for further details) We find that with increasing pressure we transition to the right towards the SL phase, see Fig. 1a.

To further strengthen our structural understanding of the system under pressure, we collected infrared absorbance spectra as a function of quasi-hydrostatic pressure at two temperature regimes 14 - 18 K and 100 K, see Fig. 3. Besides many constraints (see methods), we can observe the behavior of most of the phonon modes. Recently we reported the temperature dependence of ambient-pressure spectra³⁵, which shows an appearance of additional modes with small intensity in the spectral range dominated by the H motion below 32 K, for example in the range $3200 - 3500 \text{ cm}^{-1}$. A similar situation is found while applying pressure, if we compare the 14-18 K and 100 K absorbance spectra in Fig. 3 in the mentioned $3200 - 3500 \text{ cm}^{-1}$ range. Since there is no abrupt change in the pressure dependence at constant temperature for both cases, we can conclude that this structural modification exists when cooling through the transition below 33 K even up to the highest pressure of 10 GPa. From the application of hydrostatic pressure, we observe both red and blue shifts of the phonon modes. This is expected, when we have a lot of free structural parameters (low crystal symmetry), which are not necessarily linked to their volume dependence, see the dotted lines in Fig. 3. We divide regions of activity of different types of atoms as in Ref.³⁵ and highlight them by black arrows at the bottom of Fig. 3, their shift is given by the grey dashed lines. Region 2 is dominated by the motion of Cu and O atoms while regions 3 and 4 are dominated by H and O motions. In regions 3 and 4 we can easily find both blue and red shifts, but the phonon modes in region 2 exhibit only blue shifts, as the Cu-O bonds create the “skeleton” of the crystal structure and

are responsible for the formation of the kagome lattice of Cu^{2+} atoms. The H movement is not so strict, because it is bonded only to one atom and its position is less constrained, which agrees with the observation of blue and redshifts.

We estimate the Grüneisen parameter γ Ref.³⁶, which assumes that the atomic free volume is linked to the volume of the unit cell V leading to the relation $\gamma = -\frac{V}{v} \frac{dv}{dV}$. The details and results of such fits are shown in the Supporting materials. The dependence $v - v_{0.1\text{GPa}} = a$ together with the unit cell volume is shown in Fig. 4a. The $v(V)$ dependence is then shown in panel b, which leads to a linear dependence proving the direct link of Cu O modes to the unit cell volume. With the average frequency of 459 cm^{-1} and volume of 2150 \AA^3 we find $\gamma = 0.85$. Since we have two Cu and three O Wyckoff positions we have five different Cu-O bonds. Thus individual modes in region 2 will have slightly different pressure dependence of their positions as can be seen from Fig.s SS3 and SS4, but their blue shift is quite robust. Summarized, the skeleton of the Cu-O lattice remains mainly unchanged besides our details observed via XRD. Among the pressure range, no splittings or disappearance of phonon modes are observed via pressure considering region 3 and 4, even no unresolved H transitions exist.

Next, as a local spectroscopic technique μSR has unique sensitivity to even tiny internal fields. As such, it is commonly used as a stringent test for the absence of static magnetism in SL materials³⁷. Previous μSR measurements at ambient pressure²⁹ on a single-crystal of $\text{Y}_3\text{Cu}_9(\text{OH})_{19}\text{Cl}_8$ revealed a bulk magnetic phase transition at 2.1 K, in agreement with our NMR studies^{29,30}. Intriguingly, the internal field at base temperature was found to be broadly distributed and strikingly small, approximately 8.6 mT ²⁹. Thus zero-field μSR results suggest a strongly reduced static moment for Cu^{2+} , estimated to less than $0.1 \mu_B$ in the fully ordered phase, while in-field ^1H NMR rather points to a full moment³⁰. To investigate for a possible instability of the ordered ground state, we present below our μSR measurements conducted under pressure in zero-field (ZF) setup depicted in Fig. 5 a. In such a setup, a fraction f of muons stop in the cell's thick walls, with 50% to 70% being typical³⁸. This leads to an additional dominant background contribution from the cell besides the one of the sample (see dotted line in Fig. 5b). The functional form of this background contribution $P_{\text{cell}}(t)$ is well-known and described in Ref.³⁸. It consists of a Kubo-Toyabe function multiplied by an exponential decay. This enables a clear separation of the sample contribution from that of the cell upon data analysis. Fig. 5b compares the ZF μSR time spectra measured at ambient pressure, 1.14 GPa, 1.8 GPa, and at 2.3 GPa at base temperature of 0.28 K. At ambient pressure, a characteristic 'dip' is observed at $0.4 \mu\text{s}$ in the spectrum, as a signature of the magnetic transition in Y-Kapellasite, in line with Ref.²⁹. Thus, to determine the fraction $f = 0.53$ of the cell contribution, we combined it with the known sample response at ambient pressure and base temperature from Ref.²⁹, *i.e.* using a damped oscillatory component $\frac{2}{3} \cos(\omega_f t + \phi) e^{-\frac{\sigma_f^2 t^2}{2}} + \frac{e^{-\lambda_f t}}{3}$, where ω_f represents the muon spin precession proportional to the internal field in which it rotates, σ_f accounts for the distribution of the field, and λ_f is the relaxation rate of the '1/3' tail.

As pressure is increased, this dip vanishes and the relaxation of the asymmetry slows down remarkably, pointing to the suppression of magnetic order towards a dynamical ground state. To track this striking evolution of the relaxation rate in zero field versus applied pressure and temperature in a unified manner, with a limited number of fitting parameters, we adopted the following simplified model for the asymmetry,

$$a(t) = A_0 \left[f P_{\text{cell}}(t) + (1-f)(f_r e^{-(\lambda t)^\alpha} + (1-f_r)) \right] \quad (2)$$

where $A_0 \sim 0.3$ is the initial asymmetry. The fraction f of the signal attributed to the pressure cell remains approximately 0.54(2) across all pressures and temperatures as expected. The second part, stretched exponential, describes the muon decay asymmetry in the sample with $1/\lambda$ as the time when it relaxes to $1/e$, independent of α , while $(1-f_r) = 0.25$ stands for a minority fraction of weakly relaxing muons^{28,29}. The relaxation rate λ quantifies the relaxation across all temperatures and applied pressures (Fig. 5d). At all pressures, for $T \gtrsim 2.2 \text{ K}$, the electronic Cu^{2+} spins fluctuate fast and yield no sizeable relaxation due to motional narrowing. Therefore, the relaxation is largely dominated by weak quasi-static fields from the nuclear spins and λ is temperature-independent. At ambient pressure, the order parameter ω_f increases sharply below $T_N = 2.2 \text{ K}$ ²⁹, signaling the onset of long-range order (LRO) with the development of static internal fields, in agreement with the mean-field-like NMR line splitting³⁰. As pressure increases, the onset of accelerated relaxation of the asymmetry shifts to lower temperatures. Besides, the relaxation at base temperature is also strongly reduced with pressure. If we plot these values $\lambda(T \rightarrow 0)$ against the applied pressure, we observe a linear decrease in relaxation rate as illustrated in Fig. 5e. This trend indicates a complete suppression of muon spin depolarisation by the electronic spins around 3.5 GPa, a limit which would correspond to the case of a fully gapped SL ground state, hence no magnetic excitations at $T \rightarrow 0$. This gives evidence that pressure destabilizes LRO in Y-Kapellasite, possibly towards an entangled ground state. At the maximum pressure 2.3 GPa attainable in our experiments, the weak and smooth evolution of $\lambda(T)$ departs clearly from that of an order parameter and rather resembles the slowing down of dynamical fluctuations often observed in SL candidates, leveling off to a so-called dynamical plateau^{7,39,40}.

To further investigate the suppression of the magnetic transition under pressure and establish that the low-temperature spin correlations become fully dynamic, we now assess longitudinal field (LF) measurements, with the experimental configuration depicted in Fig. 6a. Longitudinal fields H_{LF} higher than 0.01 T fully decouple the pressure cell asymmetry³⁸, which then contributes merely as a constant background signal, as well as the nuclear relaxation from the sample. Therefore in Fig 6 b the

relaxation is due to the electronic spins of the sample in isolation. We could model the longitudinal field asymmetries at various fields at 2.3 GPa using the dynamical Kubo-Toyabe (DKT) model⁴¹ with

$$a_{LF}(t) = (A_0 - A_{bkg})P_{DKT}(t, \nu, \Delta, H_{LF}) + A_{bkg} \quad (3)$$

where the relaxation arises from a Gaussian field distribution of width Δ/γ_μ , fluctuating at a rate ν . Thus, the DKT model provides a continuous description from quasi-static disordered magnetism for $\nu < \Delta$ to a purely fluctuating regime for $\nu > \Delta$. A_{bkg} accounts for the muon stopping in the pressure cell and the small fraction of muon stopping in the sample which experience weak internal fields, effectively acting as a constant baseline for the asymmetry. Longitudinal field fits using the DKT model at 100 G, 200 G, and 500 G yield $\Delta/\gamma_\mu = 2.9$ mT, so $\Delta = 2.41(3)$ MHz and $\nu = 7.81(2)$ MHz. Since $\nu > \Delta$, the pressure of 2.3 GPa clearly manifests a dynamic ground state and the complete absence of spin freezing. At intermediate pressure, the DKT model fails to provide an accurate fit, likely due to the presence of a partially frozen state, as shown in the supplemental material. The LF fits points nonetheless at a reduction of the dynamics at lower applied pressure towards static magnetism.

The gradual transition from the ordered state to the dynamical state is illustrated in Fig. 6 c where the effect of a 0.01 T LF at 0.28 K is shown for 4 different pressures. In this LF, as explained before, the relaxation is due to the electronic spins of the sample in isolation. This simpler response evolves from a gaussian-like form at ambient pressure to an exponential one at 2.3 GPa, in agreement with an evolution from static to dynamical magnetism with applied pressure. The LF data are thus modeled using the following equation:

$$a(t) = (A_0 - A_{bkg}) \left[f_D e^{-\lambda_L t} + (1 - f_D) e^{-\frac{(\sigma t)^2}{2}} \right] + A_{bkg} \quad (4)$$

In this equation, f_D represents the dynamic fraction of the spins characterized by an exponential relaxing rate λ_L , while the other component describes the static ordered part, which follows a Gaussian-like decay term with the relaxation parameter σ . As pressure is increased from zero to 2.3 GPa, the static fraction decreases while the dynamic fraction increases, particularly observed at 1.14 GPa and 1.8 GPa. At 2.3 GPa, the muon asymmetry can be completely modeled by the exponential term, reflecting a fully dynamic case, in line with the former analysis of the decoupling LF experiment.

Thus, the ZF and LF measurements, confirm the absence of magnetic freezing and indicate that only dynamic fluctuations are present as pressure increases, clearly suggesting the presence of a SL ground state in line with our structural observation of increase of frustration.

To conclude, we realize the first controlled suppression of magnetic order approaching a spin liquid state, which we achieved by a comprehensive combination of x-ray, optical spectroscopy and μ SR measurements under hydrostatic pressure. Our work establishes Y-Kapellasite as an archetype platform to study the rise and fall of frustrated magnetism in a clean system without disorder. Exploring this material in more detail and performing similar experimental endeavours on other frustrated materials constitutes a major step forward towards the realization of the long sought-for quantum spin liquid.

References

1. Shimizu, Y., Miyagawa, K., Kanoda, K., Maesato, M. & Saito, G. Spin liquid state in an organic mott insulator with a triangular lattice. *Phys. Rev. Lett.* **91**, 107001, DOI: [10.1103/physrevlett.91.107001](https://doi.org/10.1103/physrevlett.91.107001) (2003).
2. Pinterić, M. *et al.* Anisotropic charge dynamics in the quantum spin-liquid candidate κ -(BEDT-TTF)₂Cu₂(CN)₃. *Phys. Rev. B* **90**, 195139, DOI: [10.1103/physrevb.90.195139](https://doi.org/10.1103/physrevb.90.195139) (2014).
3. Dressel, M. *et al.* Lattice vibrations of the charge-transfer salt κ -(BEDT-TTF)₂Cu₂(CN)₃: Comprehensive explanation of the electrodynamic response in a spin-liquid compound. *Phys. Rev. B* **93**, 081201, DOI: [10.1103/physrevb.93.081201](https://doi.org/10.1103/physrevb.93.081201) (2016).
4. Miksch, B. *et al.* Gapped magnetic ground state in quantum spin liquid candidate κ -(BEDT-TTF)₂Cu₂(CN)₃. *Science* **372**, 276–279, DOI: [10.1126/science.abc6363](https://doi.org/10.1126/science.abc6363) (2021).
5. Komatsu, T., Matsukawa, N., Inoue, T. & Saito, G. Realization of Superconductivity at Ambient Pressure by Band-Filling Control in κ -(BEDT-TTF)₂Cu₂(CN)₃. *J. Phys. Soc. Jpn.* **65**, 1340–1354, DOI: [10.1143/jpsj.65.1340](https://doi.org/10.1143/jpsj.65.1340) (1996).
6. Pustogow, A. Thirty-Year Anniversary of κ -(BEDT-TTF)₂Cu₂(CN)₃: Reconciling the Spin Gap in a Spin-Liquid Candidate. *Solids* **3**, 93–110, DOI: [10.3390/solids3010007](https://doi.org/10.3390/solids3010007) (2022).
7. Mendels, P. *et al.* Quantum magnetism in the paratacamite family: towards an ideal kagomé lattice. *Phys. review letters* **98**, 077204, DOI: [10.1103/PhysRevLett.98.077204](https://doi.org/10.1103/PhysRevLett.98.077204) (2007).
8. Han, T.-H. *et al.* Correlated impurities and intrinsic spin-liquid physics in the kagome material herbertsmithite. *Phys. Rev. B* **94**, 060409, DOI: [10.1103/physrevb.94.060409](https://doi.org/10.1103/physrevb.94.060409) (2016).

9. Wang, J. *et al.* Emergence of spin singlets with inhomogeneous gaps in the kagome lattice heisenberg antiferromagnets zn-barlowite and herbertsmithite. *Nat. Phys.* **17**, 1109–1113, DOI: [10.1038/s41567-021-01310-3](https://doi.org/10.1038/s41567-021-01310-3) (2021).
10. Kremer, R. K., Bette, S., Nuss, J. & Pupal, P. Chemo-structural disorder in the kagomé spin $s = 1/2$ systems $\text{ZnCu}_3(\text{OH})_6\text{Cl}_2$ and $\text{YCu}_3(\text{OH})_6\text{Br}_2[\text{Br}_x(\text{OH})_{1-x}]$, DOI: [10.48550/ARXIV.2411.18331](https://doi.org/10.48550/ARXIV.2411.18331) (2024).
11. Khuntia, P. *et al.* Gapless ground state in the archetypal quantum kagome antiferromagnet $\text{ZnCu}_3(\text{OH})_6\text{Cl}_2$. *Nat. Phys.* **16**, 469–474, DOI: [10.1038/s41567-020-0792-1](https://doi.org/10.1038/s41567-020-0792-1) (2020).
12. Paddison, J. A. M. *et al.* Continuous excitations of the triangular-lattice quantum spin liquid YbMgGaO_4 . *Nat. Phys.* **13**, 117–122, DOI: [10.1038/nphys3971](https://doi.org/10.1038/nphys3971) (2016).
13. Li, Y. *et al.* Muon Spin Relaxation Evidence for the U(1) Quantum Spin-Liquid Ground State in the Triangular Antiferromagnet YbMgGaO_4 . *Phys. Rev. Lett.* **117**, 097201, DOI: [10.1103/physrevlett.117.097201](https://doi.org/10.1103/physrevlett.117.097201) (2016).
14. Zhu, Z., Maksimov, P. A., White, S. R. & Chernyshev, A. L. Disorder-Induced Mimicry of a Spin Liquid in YbMgGaO_4 . *Phys. Rev. Lett.* **119**, 157201, DOI: [10.1103/physrevlett.119.157201](https://doi.org/10.1103/physrevlett.119.157201) (2017).
15. Balz, C. *et al.* Physical realization of a quantum spin liquid based on a complex frustration mechanism. *Nat. Phys.* **12**, 942–949, DOI: [10.1038/nphys3826](https://doi.org/10.1038/nphys3826) (2016).
16. Banerjee, A. *et al.* Neutron scattering in the proximate quantum spin liquid $\alpha\text{-RuCl}_3$. *Science* **356**, 1055–1059, DOI: [10.1126/science.aah6015](https://doi.org/10.1126/science.aah6015) (2017).
17. Mi, X. *et al.* Stacking faults in $\alpha\text{-RuCl}_3$ revealed by local electric polarization. *Phys. Rev. B* **103**, 174413, DOI: [10.1103/physrevb.103.174413](https://doi.org/10.1103/physrevb.103.174413) (2021).
18. Zhang, H. *et al.* Stacking disorder and thermal transport properties of $\alpha\text{-RuCl}_3$. *Phys. Rev. Mater.* **8**, 014402, DOI: [10.1103/physrevmaterials.8.014402](https://doi.org/10.1103/physrevmaterials.8.014402) (2024).
19. Kitagawa, K. *et al.* A spin–orbital-entangled quantum liquid on a honeycomb lattice. *Nature* **554**, 341–345, DOI: [10.1038/nature25482](https://doi.org/10.1038/nature25482) (2018).
20. Bette, S. *et al.* Solution of the heavily stacking faulted crystal structure of the honeycomb iridate $\text{H}_3\text{LiIr}_2\text{O}_6$. *Dalton Transactions* **46**, 15216–15227, DOI: [10.1039/c7dt02978k](https://doi.org/10.1039/c7dt02978k) (2017).
21. Mirebeau, I. *et al.* Pressure-induced crystallization of a spin liquid. *Nature* **420**, 54–57, DOI: [10.1038/nature01157](https://doi.org/10.1038/nature01157) (2002).
22. Kermarrec, E. *et al.* Ground state selection under pressure in the quantum pyrochlore magnet $\text{Yb}_2\text{Ti}_2\text{O}_7$. *Nat. Commun.* **8**, DOI: [10.1038/ncomms14810](https://doi.org/10.1038/ncomms14810) (2017).
23. Mirebeau, I., Goncharenko, I., Cao, H. & Forget, A. Magnetic order in $\text{Tb}_2\text{Sn}_2\text{O}_7$ under high pressure: From ordered spin ice to spin liquid and antiferromagnetic order. *Phys. Rev. B* **80**, 220407, DOI: [10.1103/physrevb.80.220407](https://doi.org/10.1103/physrevb.80.220407) (2009).
24. Stahl, Q. *et al.* Pressure-tuning of $\alpha\text{-RuCl}_3$ towards a quantum spin liquid. *Nat. Commun.* **15**, DOI: [10.1038/s41467-024-52169-w](https://doi.org/10.1038/s41467-024-52169-w) (2024).
25. Malavi, P. *et al.* Pressure-induced tuning of quantum spin liquid state in $\text{ZnCu}_3(\text{OH})_6\text{Cl}_2$. *Phys. Rev. B* **101**, 214402, DOI: [10.1103/physrevb.101.214402](https://doi.org/10.1103/physrevb.101.214402) (2020).
26. Barthélemy, Q. Etudes par RMN, μSR et chaleur spécifique de liquides de spins quantiques dans des matériaux à géométrie kagome. Electrons fortement corrélés. *Thesis, Univ. Paris-Saclay, Français* (2020).
27. Pupal, P. *et al.* Strong magnetic frustration in $\text{Y}_3\text{Cu}_9(\text{OH})_{19}\text{Cl}_8$: a distorted kagome antiferromagnet. *J. Mater. Chem. C* **5**, 2629–2635, DOI: [10.1039/c6tc05110c](https://doi.org/10.1039/c6tc05110c) (2017).
28. Barthélemy, Q. *et al.* Local study of the insulating quantum kagome antiferromagnets $\text{YCu}_3(\text{OH})_6\text{O}_x\text{Cl}_{3-x}$ ($x=0,1/3$). *Phys. Rev. Mater.* **3**, 074401, DOI: [10.1103/physrevmaterials.3.074401](https://doi.org/10.1103/physrevmaterials.3.074401) (2019).
29. Chatterjee, D. *et al.* From spin liquid to magnetic ordering in the anisotropic kagome Y-kapellasite $\text{Y}_3\text{Cu}_9(\text{OH})_{19}\text{Cl}_8$: A single-crystal study. *Phys. Rev. B* **107**, 125156, DOI: [10.1103/physrevb.107.125156](https://doi.org/10.1103/physrevb.107.125156) (2023).
30. Wang, J. *et al.* Controlled frustration release on the kagome lattice by uniaxial-strain tuning. *Phys. Rev. Lett.* **131**, 256501, DOI: [10.1103/physrevlett.131.256501](https://doi.org/10.1103/physrevlett.131.256501) (2023).
31. Zeng, Z. *et al.* Possible Dirac quantum spin liquid in the kagome quantum antiferromagnet $\text{YCu}_3(\text{OH})_6\text{Br}_2[\text{Br}_x(\text{OH})_{1-x}]$. *Phys. Rev. B* **105**, L121109, DOI: [10.1103/PhysRevB.105.L121109](https://doi.org/10.1103/PhysRevB.105.L121109) (2022).
32. Liu, J. *et al.* Gapless spin liquid behavior in a kagome Heisenberg antiferromagnet with randomly distributed hexagons of alternate bonds. *Phys. Rev. B* **105**, 024418, DOI: [10.1103/physrevb.105.024418](https://doi.org/10.1103/physrevb.105.024418) (2022).

33. Zeng, Z. *et al.* Spectral evidence for dirac spinons in a kagome lattice antiferromagnet. *Nat. Phys.* **20**, 1097–1102, DOI: [10.1038/s41567-024-02495-z](https://doi.org/10.1038/s41567-024-02495-z) (2024).
34. Hering, M. *et al.* Phase diagram of a distorted kagome antiferromagnet and application to Y-kapellasite. *npj Comput. Mater.* **8**, 1–10, DOI: [10.1038/s41524-021-00689-0](https://doi.org/10.1038/s41524-021-00689-0) (2022).
35. Doležal, P. *et al.* Lattice dynamics of the frustrated kagome compound y-kapellasite. *Phys. Rev. B* **110**, DOI: [10.1103/physrevb.110.174445](https://doi.org/10.1103/physrevb.110.174445) (2024).
36. Grüneisen, E. Theorie des festen zustandes einatomiger elemente. *Annalen der Physik* **344**, 257–306 (1912).
37. Hillier, A. D. *et al.* Muon spin spectroscopy. *Nat Rev Methods Primers* **2**, 4, DOI: [10.1038/s43586-021-00089-0](https://doi.org/10.1038/s43586-021-00089-0) (2022).
38. Khasanov, R. *et al.* High pressure research using muons at the paul scherrer institute. *High Press. Res.* **36**, 140–166 (2016).
39. Orain, J. *et al.* μ sr study of a quantum spin liquid candidate: the $s = 1/2$ vanadium oxyfluoride kagome antiferromagnet. In *Journal of Physics: Conference Series*, vol. 551, 012004 (IOP Publishing, 2014).
40. Fåk, B. *et al.* Kapellasite: A kagome quantum spin liquid with competing interactions. *Phys. review letters* **109**, 037208, DOI: [10.1103/PhysRevLett.109.037208](https://doi.org/10.1103/PhysRevLett.109.037208) (2012).
41. Hayano, R. S. *et al.* Zero and Low Field Spin Relaxation Studied by Positive Muons. *Phys. Rev. B* **20**, 850, DOI: [10.1103/PhysRevB.20.850](https://doi.org/10.1103/PhysRevB.20.850) (1979).
42. Mezouar, M. *et al.* The high flux nano-x-ray diffraction, fluorescence and imaging beamline id27 for science under extreme conditions on the esrf extremely brilliant source. *High Press. Res.* 1–28 (2024).
43. Garbarino, G. *et al.* Extreme conditions x-ray diffraction and imaging beamline id15b on the esrf extremely brilliant source. *High Press. Res.* **44**, 199–216 (2024).
44. Celeste, A., Borondics, F. & Capitani, F. Hydrostaticity of pressure-transmitting media for high pressure infrared spectroscopy. *High Press. Res.* **39**, 608–618, DOI: [10.1080/08957959.2019.1666844](https://doi.org/10.1080/08957959.2019.1666844) (2019).
45. Khasanov, R. Perspective on muon-spin rotation/relaxation under hydrostatic pressure. *J. Appl. Phys.* **132**, DOI: [10.1063/5.0119840](https://doi.org/10.1063/5.0119840) (2022).
46. Boldrin, D. *et al.* Haydeelite: A spin-1/2 kagome ferromagnet. *Phys. Rev. B* **91**, 220408, DOI: [10.1103/physrevb.91.220408](https://doi.org/10.1103/physrevb.91.220408) (2015).
47. Kermarrec, E. *et al.* Spin dynamics and disorder effects in the $s = 1/2$ kagome heisenberg spin-liquid phase of kapellasite. *Phys. Rev. B* **90**, 205103, DOI: [10.1103/physrevb.90.205103](https://doi.org/10.1103/physrevb.90.205103) (2014).

Methods

Synthesis

Single-crystal growth is realized by slowly dissolving CuO in a $\text{YCl}_3\text{-H}_2\text{O}$ solution and transporting it to the cold end. For this 4 g $\text{YCl}_3\text{-6H}_2\text{O}$, 2.3 g of CuO (Alfa Aesar, 99.9%) and 5.5 ml H_2O were transferred in a quartz ampule with outer diameter of 30 mm and an inner one of 24 mm. The growth is executed in a three zone furnace with a gradient of 30°C and a temperature of 240°C at the hot end (note that the elevated pressure at this temperature requires especially thick quartz ampules). The gradient was optimized as too low temperatures yielded a mixture of Y-Kapellasite and Clinoatacamite. After 7 months the inclusion-free hexagonal single-crystals have an average size of $3 \times 3 \times 1 \text{ mm}^3$ up to $4 \times 4 \times 2 \text{ mm}^3$.

Diffraction

Single crystal XRD data under applied pressure at all temperatures were collected at the beamline ID27⁴² and the low temperature data at ambient pressure at ID15B⁴³ of the European Synchrotron Radiation Facility (ESRF). We used membrane driven diamond anvil cells and helium as the pressure transmitting medium. Natural single crystalline diamonds with Boehler-Almax cut culets of $500 \mu\text{m}$ in size were mounted on seats with a modified Boehler-Almax design and an opening of 70° . Stainless steel was used as gasket material. $200 \mu\text{m}$ thick plates were pre-indented to $100 \mu\text{m}$. The sample chamber was created by laser drilling a hole of $300 \mu\text{m}$ in diameter. The cell was loaded with compressed He and closed at 1400 bar. The applied pressure was determined from ruby fluorescence. Room temperature data was collected in continuous ϕ rotation over 68° in shutterless readout of the EIGER2 X CdTe 9M detector (Dectris, Switzerland) in 0.25° steps. For the low temperature experiments diamond anvil cells made of CuNi_2Be were mounted in a Helium flow cryostat (ESRF) and data collected in continuous ϕ rotation over 64° . For the ambient pressure experiment at low temperature the sample was mounted on a $300 \mu\text{m}$ thick diamond plate and cooled with a small Helium flow cryostat (ESRF). Data was collected in continuous ϕ rotation over 70° in 0.25° steps. The detector distance was calibrated using CeO_2 powder to 185.5 mm for the room temperature data at ID27,

183.8 mm for low temperature at ID27 and 179.2 mm for low temperature at ID15B. The diffraction geometry was calibrated using a natural vanadinite single crystal and the flat-field of the detector was calibrated using air scattering at the employed x-ray energies. The key experimental results were obtained using monochromatic x-rays with a wavelength of 0.22290 Å for room temperature data, 0.3738 Å for low temperature at ID27 and 0.4099 Å for low temperature data at ID15B.

Optics

Pressure-dependent optical studies were carried out at SMIS beamline of Synchrotron Soleil, France. The vector of electric field was parallel with the basal plane of the unit cell, which means that only the E_u phonon modes are observable³⁵. The optical measurements in diamond anvil cells limit the accessible signal and ranges, which are not hampered by the absorption of the diamond windows. Due to the samples thickness in case of strong absorption we are losing the shape of the maxima, visible in comparison to the dotted line in Fig. 3. The spectral range below 150 cm^{-1} was not detectable due to strong water vapour absorption in the far-infrared. In this range, our ambient-pressure measurements have evidenced magneto-elastic coupling³⁵ leading to two subtle H-based structural transition below 33 K²⁹ unresolvable by XRD.

At SMIS we used a membrane driven DAC of the Le Toullec type, with Ilas diamond anvils and 500/600 μm culet, stainless steel gaskets preindented to a final thickness of about 50 μm , where a hole has been drilled by electric discharge machine. The pressure transmitting medium was Polyethylene (PE) and NaCl in the FIR and MIR ranges, respectively⁴⁴. The pressure cell was mounted in a liquid He flow cryostat equipped with BaF₂ windows for the MIR range and polypropylene ones for the FIR range. The spectra were collected with a ThermoFisher iS50 FTIR spectrometer, with synchrotron radiation as a light source, KBr (solid substrate) beamsplitter and a MCT (liquid He-cooled Si bolometer) detector for the MIR (FIR) range. The spectrometer was coupled to an in-house developed horizontal IR microscope having custom reflective Schwarzschild objectives with large working distance.

Muons

ZF, TF and LF MuSR experiments were carried out at the Paul Scherrer Institute PSI, Switzerland. Experiments under the quasi-hydrostatic pressure conditions were conducted at the MuE1 beam-line using the GPD spectrometer^{38,45}. A pressure up to 2.3 GPa was generated in a double-walled clamp type cell made of nonmagnetic MP35N alloy. As a pressure transmitting medium, Daphne 7373 oil was used. We filled the pressure cell with about 1.7 g of crushed single-crystals for the measurements. The applied pressure was determined at low temperature by measuring the superconducting transition temperature of a small piece of In placed inside the cell.

Acknowledgements

We acknowledge the ESRF within the in-house proposals IH-HC-3746 and IH-HC-4021 and SOLEIL for provision of synchrotron radiation. We acknowledge support by the Deutsche Forschungsgemeinschaft (DFG) via DR228/68-1 and TRR288 (No. 422213477, Project A03). The work of P.D. was funded by the Czech Science Foundation (research project GAČR 23-068100). A.P. acknowledges support by Hochschuljubiläumsfonds der Stadt Wien (Grant No. H-918729/2022). We acknowledge the support of the French Agence Nationale de la Recherche, under Grant No. ANR- 18-CE30-0022 “LINK”. We thank Jeroen Jacobs for preparation and gas loading of the high-pressure cells, Apostolos Pantousas for single crystal refinement support and Jenz Jakschik for measurement support at the SOLEIL beamtime.

Author contributions statement

Crystals were grown by K.M.Z. under the supervision of P.P. and C.K. single-crystal XRD under pressure was done at ESRF by P.P., T.B., G.G, F.A. and B.W., where P.P. and F.A. analyzed the data. Optical studies were conducted by T.B., G.K., S.R. and F.C., at Soleil P.D. and A.P. analyzed and interpreted the data. MuSR experiments were conducted at PSI by D.C., K.M.Z., R.K., F.B. and P.P., D.C. analyzed the data. P.P., D.C. F.B., A.P. and P.D wrote the manuscript. All authors reviewed the manuscript.

Data availability

The high-pressure x-ray diffraction data from ID27 is available at <https://doi.org/10.1515/ESRF-ES-765584497> and <https://doi.esrf.fr/10.1515/ESRF-ES-1710763903>.

Competing interests

The authors declare no competing interests.

Additional information

Supplemental material

X-ray diffraction

Y-Kapellasite crystallizes in the trigonal space group #148 $R\bar{3}$ with $a = b = 11.57 \text{ \AA}$, $c = 17,33 \text{ \AA}$, which is a subgroup and supercell of $\text{YCu}_3(\text{OH})_6\text{Cl}_3$ ¹⁰. We display the zonal (0kl) maps of diffraction of the subcell in red in Fig. S1a, which clearly differ from the supercell (see Fig. S1b,c) independent of pressure as these superstructure reflexes still are present at the highest applied pressure of 10 GPa.

Exchange interaction

In our compound we are dealing with a hydroxychloride-system, where a crossover for FM (here negative defined) to AFM (here positive) is expected around 105° ⁴⁶. For our exact case, we have two anchorpoints from our inelastic neutron scattering experiment, where we find that $J_\square \approx J = 140 \text{ K}$ and $J' = 63 \pm 7 \text{ K}$ determined at a temperature of 1.55 K ²⁹. Using our lowest temperature diffraction result summarized in Fig. 2 we know the angles of J_\square and J are 117° and 117.5° averaging to $117.25 \pm 0.25^\circ$ and J' has the angle 110.6° (see Fig. S2). Consequently we can use a linear fit to work out the change of our exchange interactions for the angles that do vary within 110 to 118° as we observe in our XRD analysis. On top we have determined in previous works for the closely related materials kapellasite $\text{ZnCu}_3(\text{OH})_6\text{Cl}_2$ an exchange interaction of -12 K ⁴⁷ with only one Cu-O-Cu bond of an angle of 105.5° and herbertsmithite $\text{ZnCu}_3(\text{OH})_6\text{Cl}_2$ an exchange interaction of 180 K ¹¹ and kagome bond angle of 118.9° ¹⁰. These additional points of related systems support the range and estimation of our exchange interactions within errorbars.

Optics

The pressure dependence of the mode frequencies ν linked to the volume is captured by the Grüneisen parameter γ Ref.³⁶ $\gamma = -\frac{V}{\nu} \frac{d\nu}{dV}$. To subtract the ν dependence of the spectral region 2 on the pressure, we took the lowest pressure data as the reference and the other pressure spectra were shifted and scaled to this reference data via $I f(\nu - a)$. I and a are free parameters for the fit. The results of such fits are shown in Fig. S3 and Fig. S4. We show for a selected frequency range the change of spectral intensity with increasing pressure at 100 K and $14\text{-}18 \text{ K}$. As we have two Cu and three O Wyckoff positions we have five different Cu-O bonds individual modes will have slightly different pressure dependence of their positions as can be seen from Fig.s S3 and S4, but their blue shift is robust.

Muons

Having successfully fitted the asymmetry at 2.3 GPa for longitudinal fields of 0.01 T , 0.02 T , and 0.05 T using the dynamical Kubo-Toyabe (DKT) model, which clearly indicates a spin liquid ground state, we extended the application of the DKT model to intermediate pressures of 1.8 GPa and 1.14 GPa . As discussed in this work, the presence of mixed frozen and dynamic phases in the intermediate pressure regime results in a gradual degradation of the fits as the pressure decreases, as shown in figure S5 a,b,c. Specifically, the fluctuation rate ν slows, while the static internal field strength, proportional to the parameter Δ , increases, as shown in Fig. S5 d. These trends continue as the system approaches ambient pressure, culminating in an ordered state.

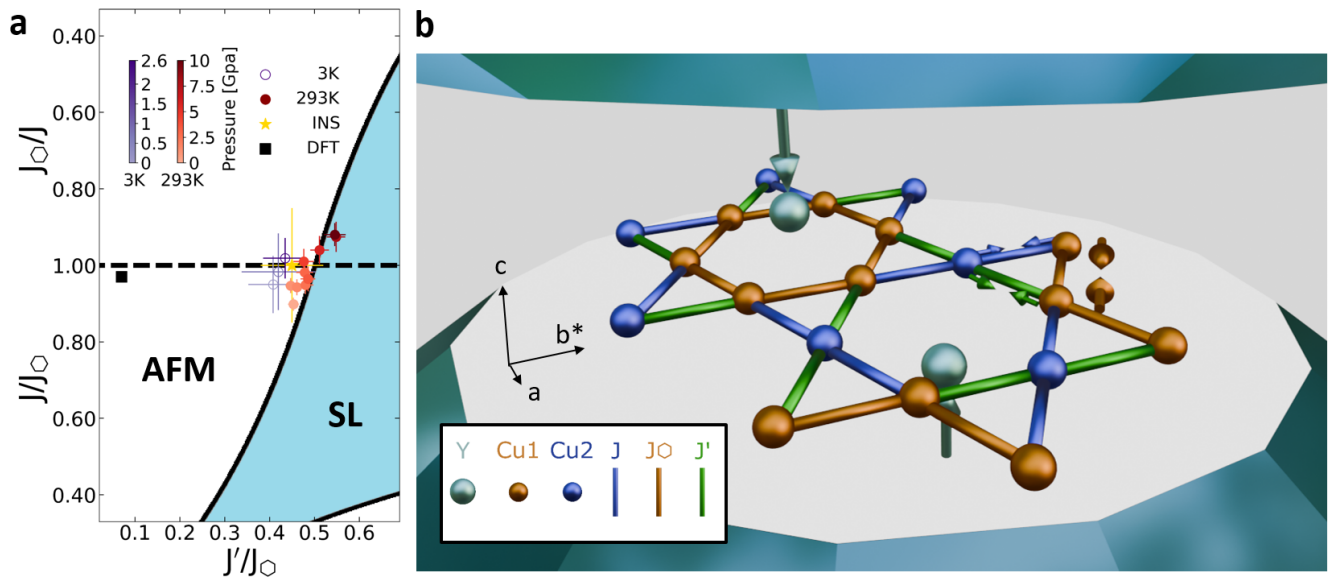


Figure 1. Pressure stabilized spin liquid. **a** Phase diagram of the distorted kagome antiferromagnet for varying exchange interactions J_0 , J and J' ³⁴ with the white area corresponding to an antiferromagnetic (AFM) type in-plane ($1/3$, $1/3$) order and blue to a SL. The DFT calculation is given as a black square³⁴ and INS results as a yellow star²⁹. In addition we estimate the exchange interactions via equation 1 (blue dots for low temperature and red dots for high temperature data), where the pressure is color-coded as given in the legend. **b** Compression sketch of the structure of Y-Kapellasite for a single layer in a diamond anvil. The atom colorcoding is given in the legend. The magnetic exchange path J_0 of the orange Cu1-Cu1 bond, J' of the green Cu1-Cu2 bond and J from the blue Cu2-Cu1 bond are indicated. The two metallic grey arrows highlight the pressure pushing the dislocated Y atoms back into the plane, which were pulled from shorter apical bonded $(\text{OH})^{-1}$ instead of Cl^{-1} (not shown) realized by the $1/9$ substitution of $\text{YCu}_3(\text{OH})_6\text{Cl}_3$ to $\text{Y}_3\text{Cu}_9(\text{OH})_{19}\text{Cl}_8$. From the pulled out Y, the Cu kagome is buckling with two Cu positions, which is tuned by the external pressure, leading to a control of the exchange interactions shown in a.

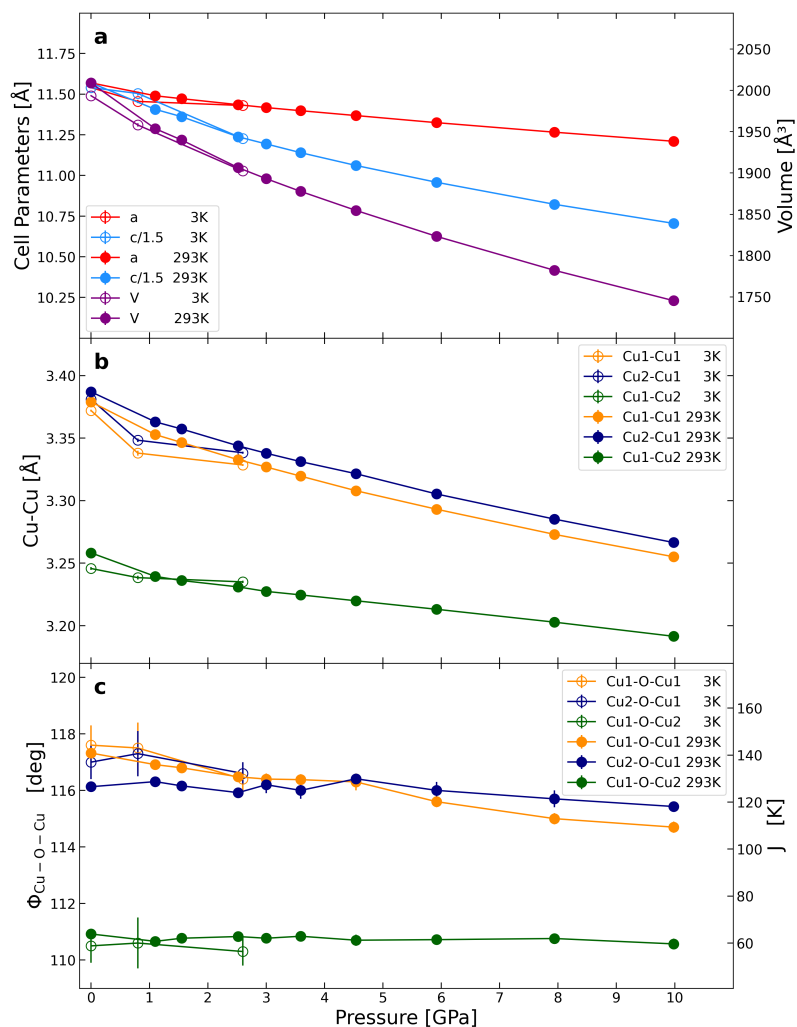


Figure 2. Pressure dependence of the single-crystal refinement results of Y-Kapellasite. **a** Lattice constants $a = b$ (red), c divided by 1.5 to fit on the same scale (blue) and the Volume change in purple with the scale shown on the right axis. **b** The bonding angle of Cu1-O-Cu1 bond (orange) corresponding to J_{\square} , Cu1-O-Cu2 bond (green) defining J' and the Cu2-O-Cu1 bond (dark blue) from J are plotted versus the external applied pressure. **c** The distances of the Cu1-Cu1 bond (orange), Cu1-Cu2 bond (green) and the Cu1-Cu2 bond (dark blue) against increasing pressure.

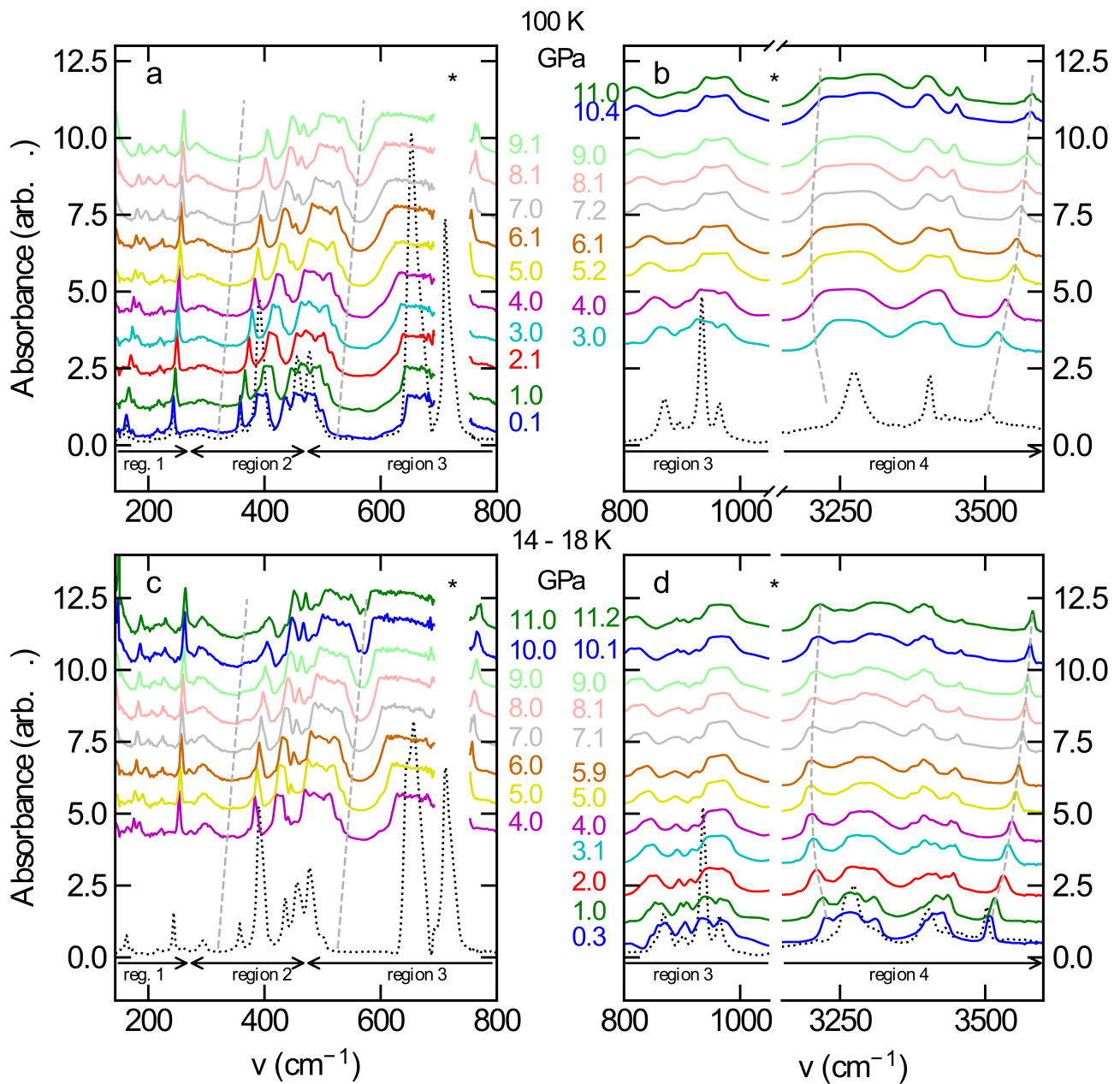


Figure 3. Pressure dependence of Absorbance. Low temperature Absorbance with increasing pressure at 100 K **a, b** and at 14-18 K **c, d**. The spectra are shifted along the y-axis to increase the clarity. The regions marked by * are excluded because of the contribution from the experimental setup. The dotted line corresponds to the ambient pressure results at 100 K and 20 K, respectively. Far (1,2) and mid-infrared (3,4) regions are indicated by horizontal double arrows separating the regions with the dominant motion of different atoms in the phonon modes. The grey dashed lines are guides for the eyes to highlight the blue and redshifts.

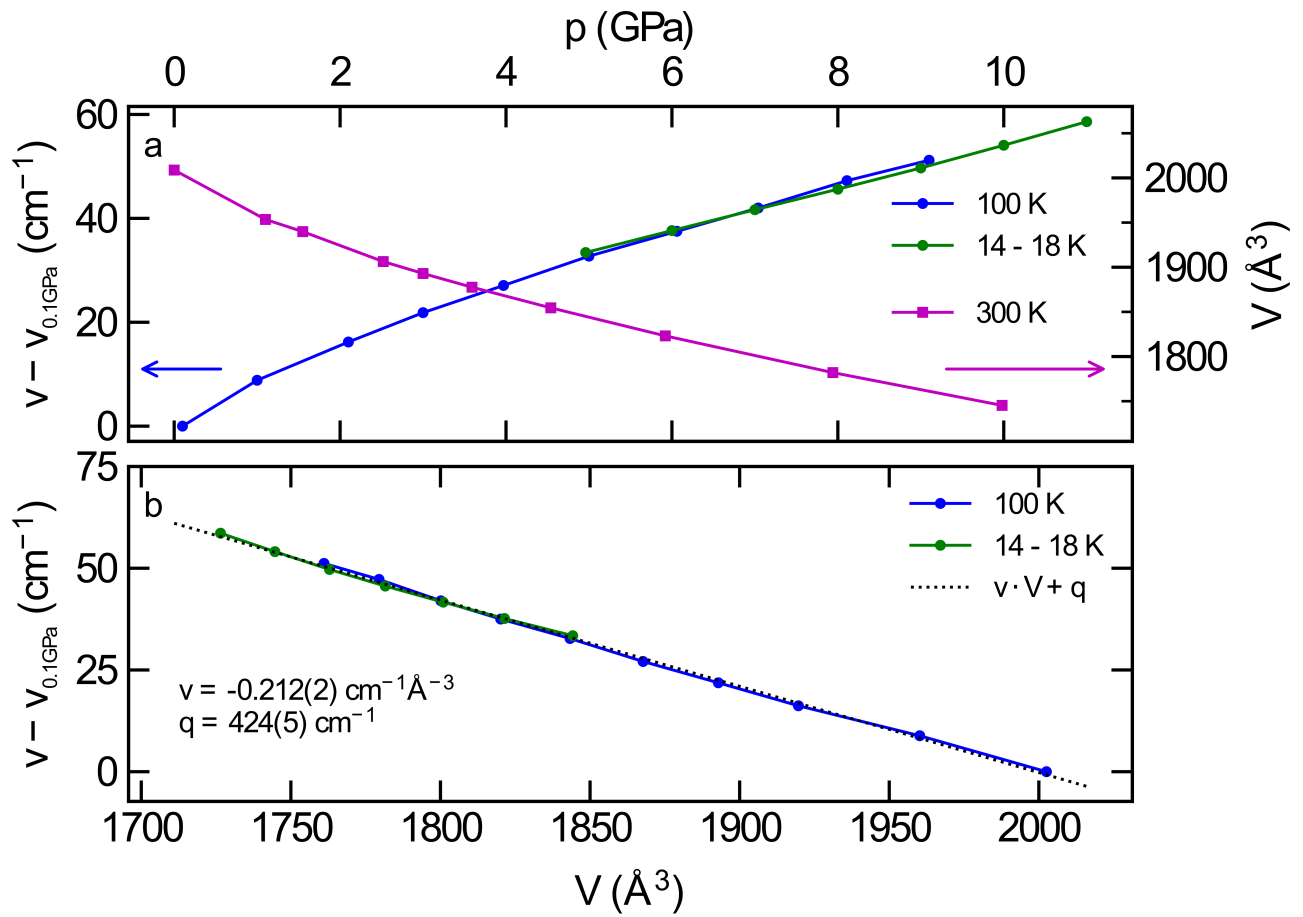


Figure 4. Phonon shift. **a** Pressure dependence of unit cell volume and shift of phonon modes in spectral region2, results of the fit (For details see the main text.). **b** The volume dependence of phonon mode shift constructed from the above plot. The dependence is fitted by a linear function.

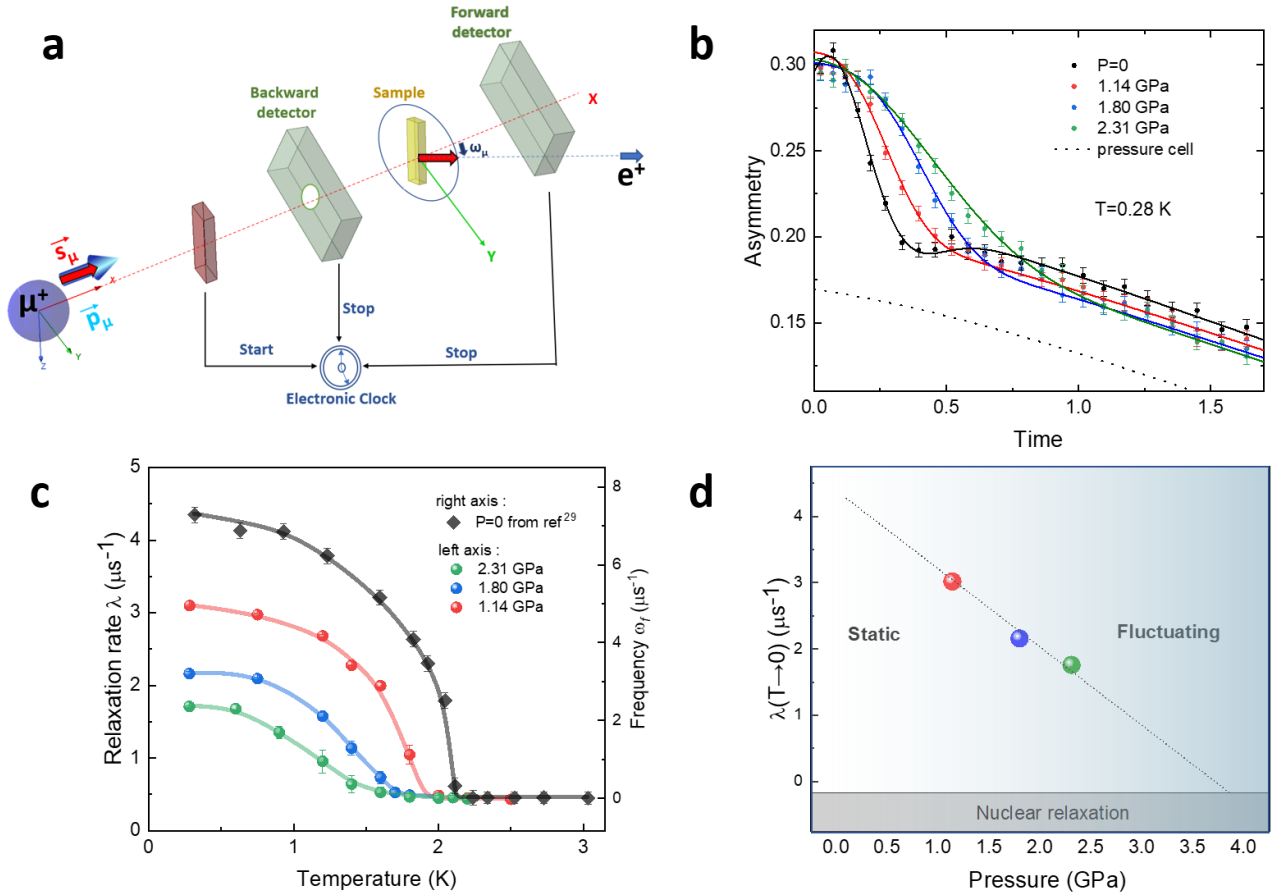


Figure 5. Pressure-dependent zero-field μ SR measurements and relaxation rates. **a** In this experimental setup, muons with an initial spin polarization \vec{s}_μ aligned with their momentum \vec{p}_μ are implanted into a sample placed between two positron detectors, designated as forward (F) and backward (B). The timing sequence starts as each muon passes through the start detector (S) and concludes when a decay positron is detected in either detector F or B. **b** ZF asymmetries at 0.28 K under different pressures: ambient pressure and 1.14 GPa, 1.8 GPa, and 2.3 GPa. The black dotted line indicates the contribution from the pressure cell. **c** Temperature evolution of the frequency (ω_f)²⁹, representing the internal field at ambient pressure, and the relaxation rate (λ) at specified pressures. **d** Relaxation rate at the lowest temperature as a function of pressure, illustrating the destabilization of the static ground state with pressure.

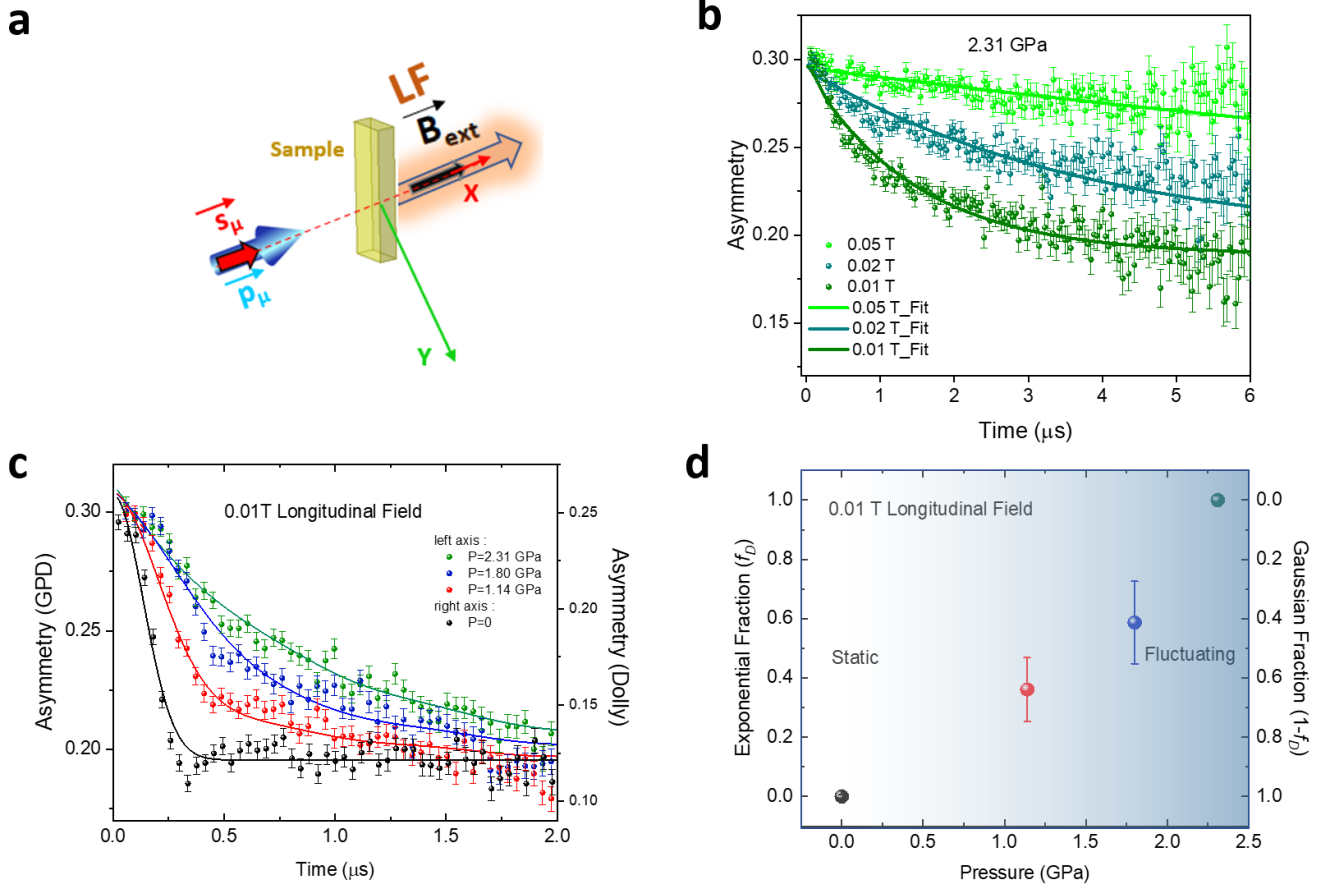


Figure 6. Pressure-dependent longitudinal-field μ SR measurements. **a** Schematics of longitudinal field (LF) setup. **b** Time evolution of LF asymmetries at 0.28 K under three different fields: 0.01 T, 0.02 T, and 0.05 T at 2.3 GPa, along with the corresponding fits to the Dynamical Kobo-Toyabe (DKT) model pointing to a dynamical ground state. **c** Muon decay asymmetries at 0.28 K and 0.01 T longitudinal field at ambient pressure, 1.14, 1.8 and 2.31 GPa with fits to equation 4. Note that the ambient pressure LF data were obtained from the Dolly instrument at PSI with no the pressure cell. Consequently, the initial asymmetry at ambient pressure is quite different from that observed at all other pressures (GPD data). **d** Evolution of the exponential f_D (dynamical) and Gaussian $1 - f_D$ (static) fractions with pressure for the fits shown in panel c using Eq. 4. At intermediate pressures (1.14 and 1.80 GPa), the system exhibits a mixed relaxation between the fully dynamic and fully static limits observed at the highest and lowest pressures in GPD. The intermediate pressures show a larger error in f_D compared to the extreme cases, where the ground state is well defined. This indicates a gradual rather than abrupt evolution of the ground state, highlighting its complexity at intermediate pressures.

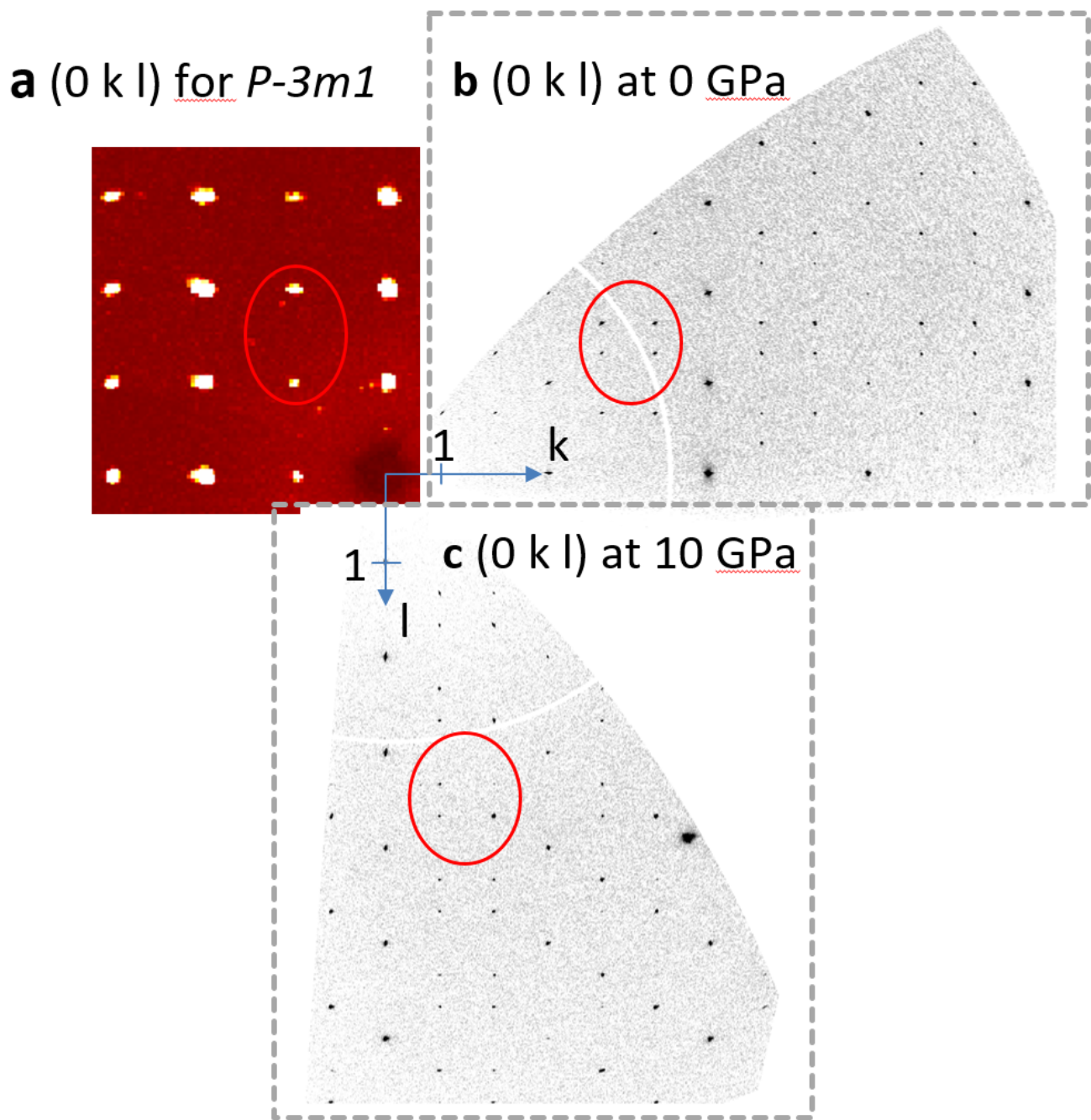


Fig. S1. Zonal diffraction maps. Zonal (0 k l) map sections of the single-crystal diffraction **a** in red for $\text{YCu}_3(\text{OH})_6\text{Cl}_3$ with the $P\bar{3}m1$ subcell and two areas of single-crystal XRD of $\text{Y}_3\text{Cu}_9(\text{OH})_{19}\text{Cl}_8$ with the supercell $R\bar{3}$ **a** at 0 GPa and **b** 10 GPa. The sections are moved and scaled such that they match the indicated k, l-axis with a uniform origin. The changing reflexes moving from sub- to supercell are highlighted via a red circle.

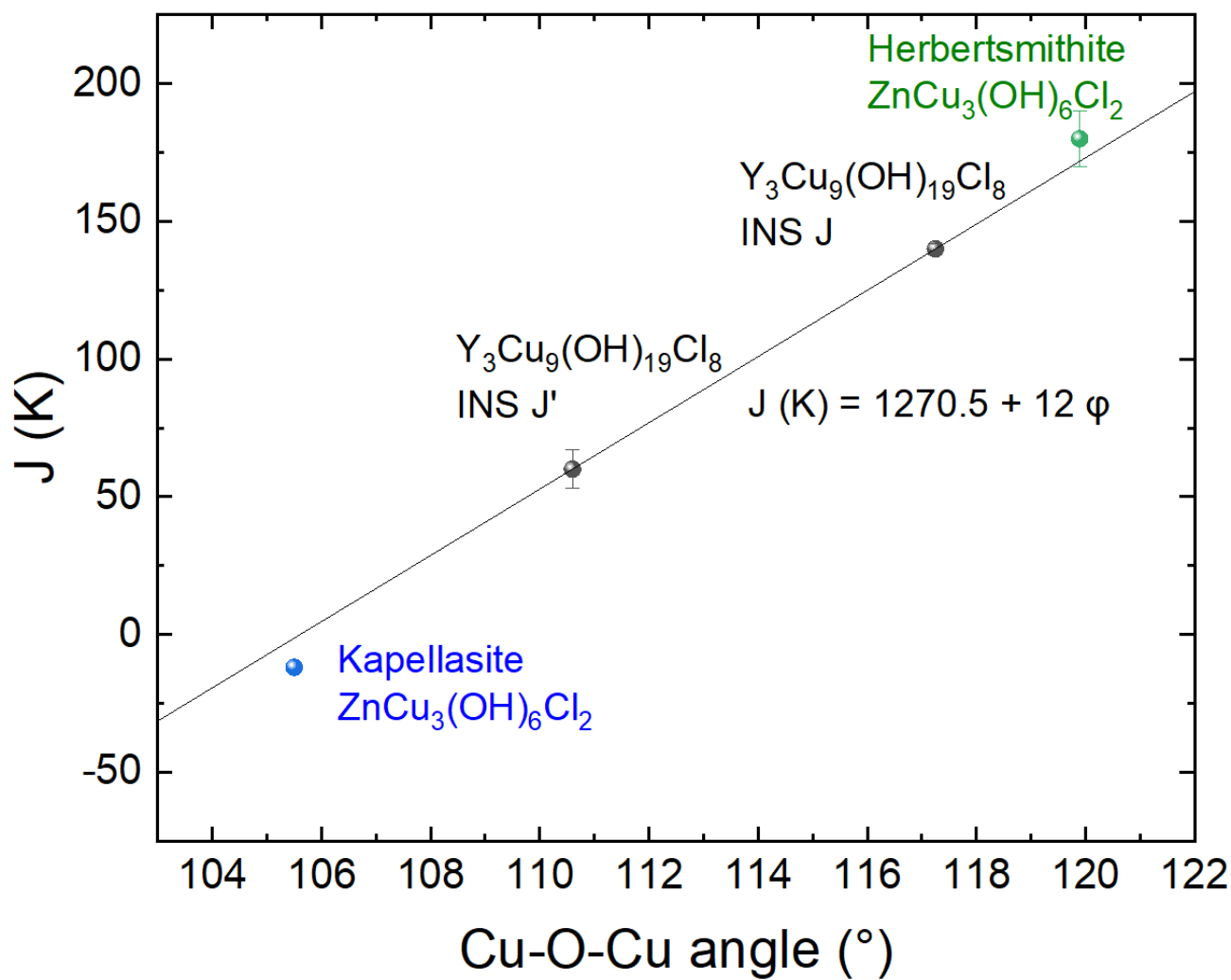


Fig. S2. Angle dependence of the J . Superexchange interaction J in Kelvin versus the copper-oxide-copper angle for Y-Kapellasite (black)²⁹ kapellasite (blue)⁴⁷ and herbertsmithite (green)¹¹.

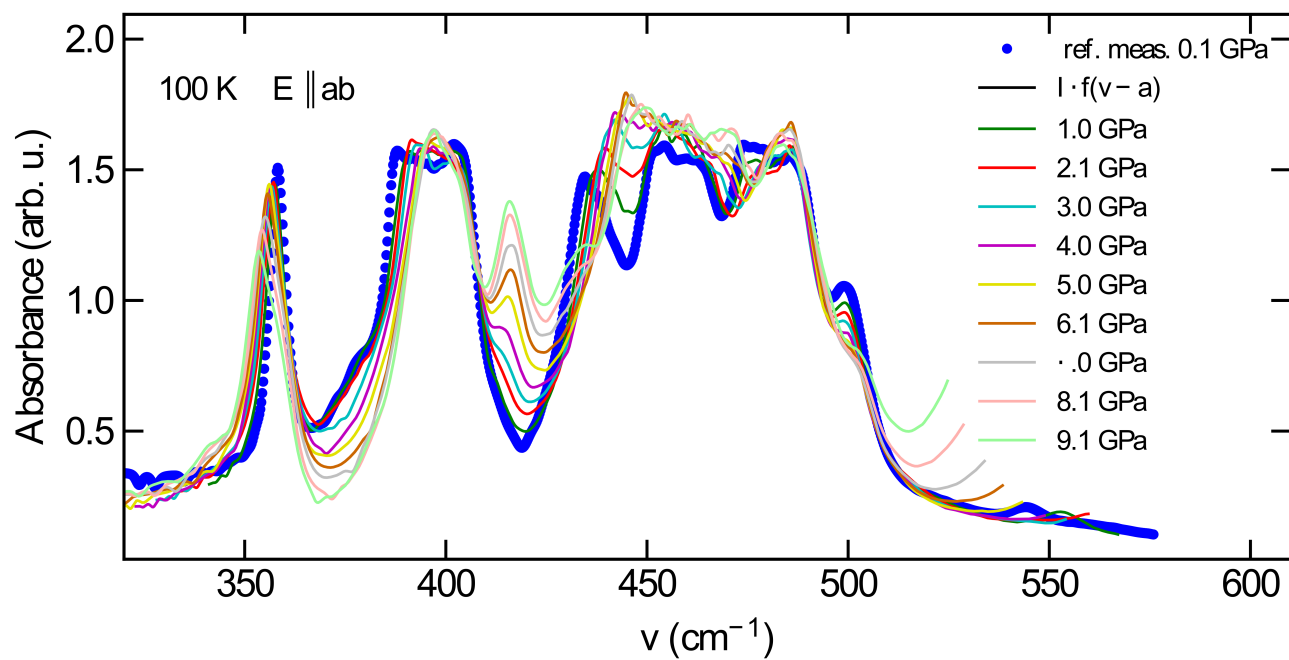


Fig. S3. High temperature low wavenumber region of the absorbance. Results of the shifted spectral intensity $I f(\nu - a)$ in region 2 at 100 K. As the reference the spectral intensity at 0.1 GPa was used. For details see the main text.

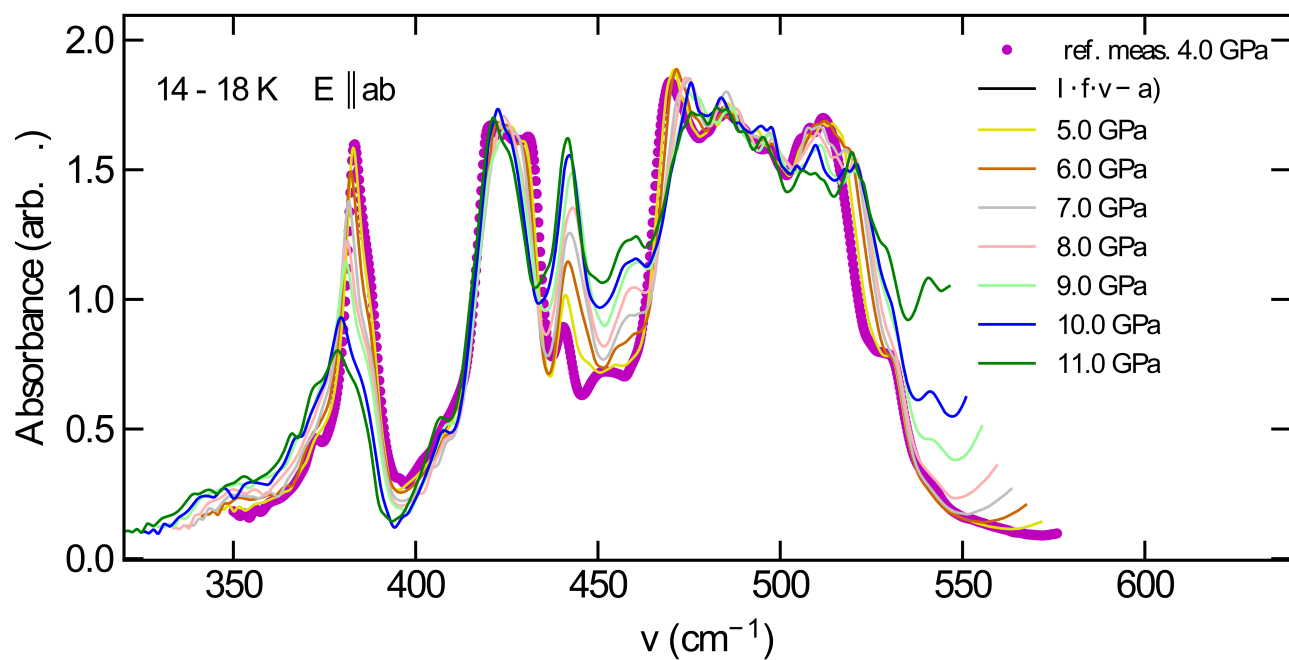


Fig. S4. Low temperature low wavenumber region of the absorbance. Results of the shifted spectral intensity $I f(\nu - a)$ in region 2 at 14-18 K. As the reference the spectral intensity at 4.0 GPa was used. For details see the main text.

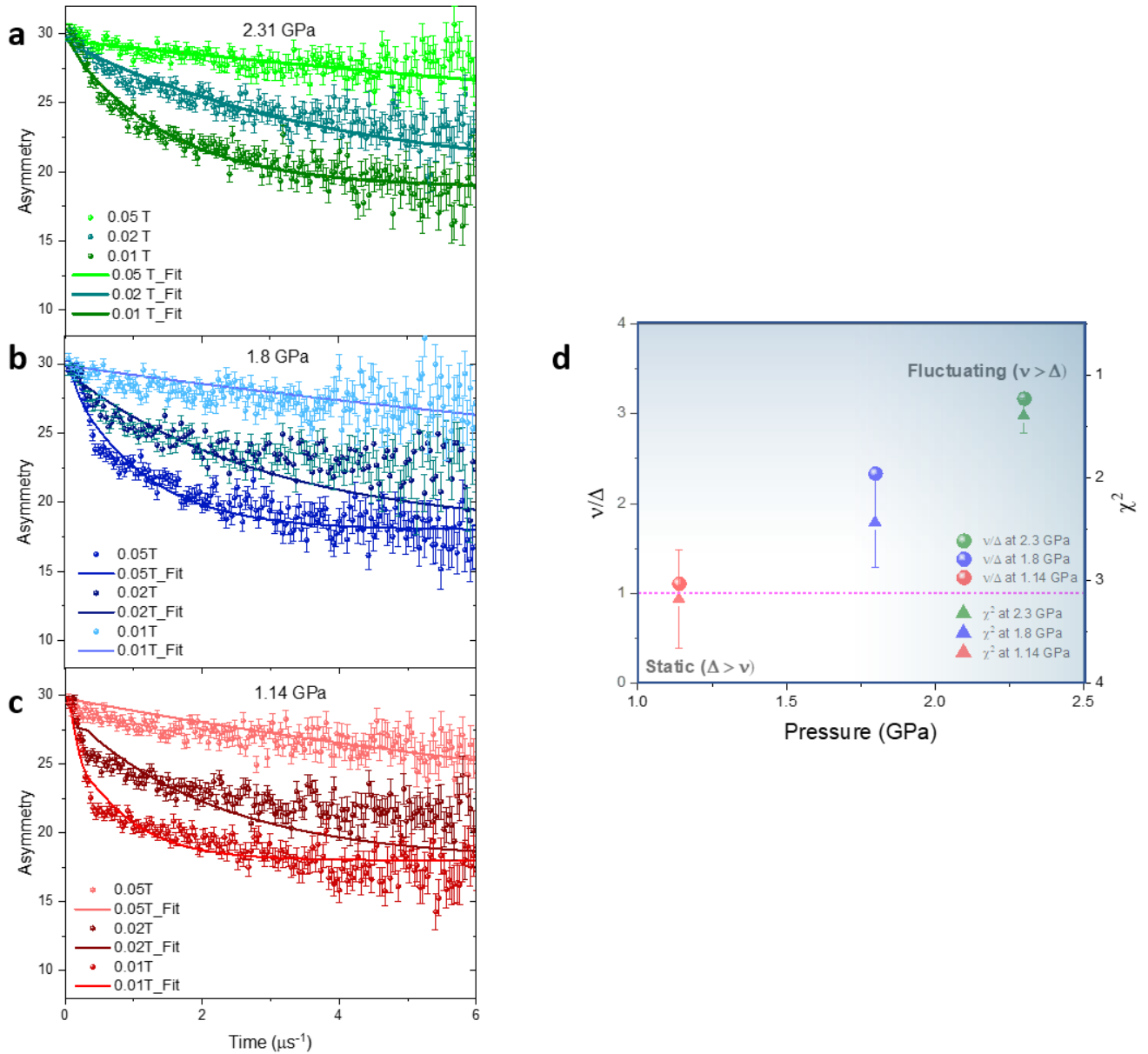


Fig. S5. Assessment of pressure-induced enhanced fluctuations using the DKT model. Asymmetry with longitudinal fields of 0.05 T, 0.02 T, and 0.01 T fitted with the DKT model at 0.28 K and at pressures: **a** 2.3 GPa, **b** 1.8 GPa, and **c** 1.14 GPa. **d** The left y-axis shows the evolution of the dynamic ground state with pressure, quantified by the ratio v/Δ , where v represents the fluctuation rate of a field distribution of width $\Delta/\gamma\mu$. The dotted violet line at $v/\Delta = 1$ marks the transition in the DKT model between dynamic and static regimes. The right y-axis depicts the deviation of the fits, represented by the χ^2 values obtained from global fits in the left panels **a**, **b** and **c**. As pressure decreases, the fit quality deteriorates. This degradation arises as the system loses dynamicity, and the Dynamic Kubo-Toyabe model fails to capture the complex relaxation (different from a simple Kubo-Toyabe) in the quasi-static ground state at lower pressures.